ChemCatChem

ChemCatChem
Chemistry Europe
European Chemical Societies Publishing

RESEARCH ARTICLE OPEN ACCESS

Gallia- Versus Alumina-Supported Cu: Dynamics of Ga in Catalysts for Green Methanol Production

Lorena Baumgarten[1,2] | Patrik Hauberg[3] | Sebastian Mangelsen[3] | Claude Coppex[2] | Jelena Jelic[2] | Mariam Lena Schulte[1,2] | Anna Wolf[3] | Bjarne Taetz[3] | Hinrich Klamor Reller[3] | Morteza Saedimarghmaleki[3] | Felix Studt[1,2] | Erisa Saraçi[1,2] | Justus Just[4] | Malte Behrens[3] | Jan-Dierk Grunwaldt[1,2]

[1]Institute for Chemical Technology and Polymer Chemistry, Karlsruhe Institute of Technology, Karlsruhe, Germany | [2]Institute of Catalysis Research and Technology, Karlsruhe Institute of Technology, Eggenstein-Leopoldshafen, Germany | [3]Institute of Inorganic Chemistry, Kiel University, Kiel, Germany | [4]MAX IV Laboratory, Lund University, Lund, Sweden

Correspondence: Malte Behrens (mbehrens@ac.uni-kiel.de) | Jan-Dierk Grunwaldt (grunwaldt@kit.edu)

Received: 29 August 2025 | **Revised:** 28 November 2025 | **Accepted:** 10 December 2025

Keywords: Cu/Ga_2O_3 | Cu/Al_2O_3 | operando XAS | operando XRPD | CO_2-hydrogenation

ABSTRACT

The transformation of CO_2 and green hydrogen into methanol presents a sustainable route for chemical and fuel production. Conventional methanol synthesis catalysts, such as $Cu/ZnO/Al_2O_3$, employ Al_2O_3 as a structural promoter, while Ga_2O_3 has recently emerged as a promising alternative. This study compares Cu-based catalysts supported on Al_2O_3 (CA) and Ga_2O_3 (CG), prepared via coprecipitation of layered double hydroxide precursors with identical molar Cu:M (M = Al or Ga) ratio of 70:30. Using in situ and operando X-ray absorption spectroscopy and X-ray powder diffraction, we investigate the structural and redox dynamics of Ga during activation and CO_2 hydrogenation. Gallium from its precursor state undergoes several phase transitions. At elevated temperatures, Ga exhibits redox activity, transitioning from Ga^{3+} to metallic Ga^0 and forming Cu_xGa_y alloys at 480 °C, followed by de-alloying and re-oxidation at even higher temperatures. Our results suggest that the beneficial role of Ga reported in literature arises from metal-oxide interfacial effects rather than bulk alloying. Excess Ga_2O_3 leads to low conversion levels and pronounced deactivation compared to the Al_2O_3-supported Cu catalyst and thus should be prevented. These findings highlight the importance of controlling promoter loading and dynamic behavior in catalyst design to optimize activity, stability, and selectivity for CO_2-to-methanol conversion.

1 | Introduction

The valorization of CO_2 has gained interest in recent years in the context of climate change, as the reaction of CO_2 and green hydrogen can yield chemicals and fuels [1, 2]. With this so-called power-to-liquid approach, methanol, which currently has a market of over 110 million tons per year [3], can be obtained in a renewable form. Nowadays, methanol is mainly synthesized from fossil-derived syngas consisting of CO, H_2, and CO_2 at 50–100 bar pressure and temperatures of 200 °C–300 °C, typically using a copper-zinc-alumina catalyst [4]. Herein, Al is used as a structural promoter as it acts as a spacer and stabilizer for the Cu particles and can furthermore electronically promote methanol formation [5]. It remains in its initial oxidation state, but can exhibit different morphologies and phases, including mixed Al–Zn phases [6]. Recently, a secondary promotional effect was suggested based on the doping of the ZnO component of the catalyst to increase its reducibility [7]. In general, the

Lorena Baumgarten and Patrik Hauberg contributed equally to this work.

benefit of Al_2O_3 in the conventional catalyst system is undeniable but rarely discussed in the literature. In contrast, the effect of Zn promotion in the conventional methanol catalyst has been intensively studied over decades, suggesting that Zn is involved in the electronic promotion of CO_2-hydrogenation based on its partial reduction [8–10]. Besides Zn and Al, Ga was identified to be promising for the synthesis of methanol using CO_2 as the feedstock [11–15]. For example, Paris et al. [12] found an increase in conversion and methanol selectivity when Cu/SiO_2 was promoted with Ga compared to Zn. A recent study by Lam et al. [15] reported a shift toward higher methanol selectivity in CO_2 hydrogenation for Ga doped Cu/SiO_2. The promotion with Ga led to an improved methanol selectivity (ca. 90%) compared to unpromoted (ca. 48%) or Zr-promoted (ca. 77%) Cu/SiO_2 catalysts. Moreover, they reported a $CuGa_x$ alloy formation upon reduction treatment, while exposure to CO_2 hydrogenation conditions resulted in de-alloying into Cu particles and Ga^{3+} sites [15]. These findings suggest that the interface of Cu^0 and Ga^{3+} is leading to higher selectivity. Gómez et al. [16], on the contrary, discarded the formation of a CuGa alloy in their Ga-doped Cu/SiO_2 catalysts, but emphasized the importance of Cu-Ga_2O_3 interaction. Kordus et al. identified a partly reduced Ga and CuGa alloy at higher temperatures for nanoparticles supported on SiO. The alloy resulted in increased selectivity toward methanol during CO_2-hydrogenation [17].

The structural promoting effect of Ga_2O_3 could be analogous to that of Al_2O_3 due to their similarity, yet a direct comparison of the promoting effect of Ga_2O_3 with its higher homologue Al is still lacking, although both are separately seen as typical—mostly structural—promotors for methanol synthesis [16, 18, 19]. Despite the similarity to Al, Ga is more redox active and can react in analogy to Zn forming partially reduced surface sites in vicinity of Cu, albeit not quite as strongly. Combining features of both Al and Zn, electronic and also structural promotion by Ga in Cu-catalysts can be expected if gallium oxide is used as a support. However, these effects may be strongly dependent on preparation, composition, and reduction history as often observed for supported catalysts. Moreover, in-depth knowledge regarding the dynamics of Cu/Ga_2O_3 catalysts in analogy to Cu/Al_2O_3 and $Cu/ZnO/Al_2O_3$ would be desirable. While for example Alfke et al. [20] studied Cu/Ga_2O_3 nanoparticles supported on SiO_2, bulk phenomena in Cu/Ga_2O_3 systems are still unknown. For CuZn-based systems, in situ and operando studies have shown that the reduction of Zn can be promoted by Cu [10, 21–25]. In particular, the electronic promotion is explained by strong metal support interaction (SMSI), which form in a self-assembled manner as reduced support species migrate onto the surface of the metal.

Less is known, however, regarding the dynamic behavior of Ga^{3+} in the presence of Cu as an alloying metal and in a reducing hydrogenation atmosphere. In NiGa-catalysts the reduction ultimately leading to alloys or intermetallics has been observed to start at 300 °C, whereas in the PdGa-based catalysts, a reduction temperature of 320 °C was found, while reduction temperatures of pure Ga are > 500 °C [26, 27]. An analogous behavior is found for the CuGa system [20]. Although synchrotron techniques have previously been used to characterize the CuGa systems for CO_2-hydrogenation to methanol [15, 20, 28], discerning the dynamics of both Cu and Ga components is challenging as features of the x-ray absorption near edge structure (XANES) at the Ga K edge do not only depend on the oxidation state, but also on the coordination geometry, i.e. the Ga^{3+} phase [29–32]. As the XANES region is often used as a fingerprint, complementary methods, like x-ray powder diffraction (XRPD), which allows the detection of crystalline phases and changes in their cell parameters, render this a strong method combination. Further, access to element-specific information would be desirable. Again, x-ray absorption spectroscopy (XAS) and XRPD are a powerful combination of techniques that can be simultaneously used at selected synchrotron facilities at relevant reaction temperatures and pressure [33–37].

In this study, we aim to investigate the speciation and dynamics of Ga in a Cu-Ga catalyst in comparison with a Cu-Al catalyst, which were prepared by the same method, thus enabling a direct structural and mechanistic comparison. In order to reduce the complexity of the system, we employ a binary Cu-M (M = Al or Ga) model system with a fixed molar Cu:M ratio of 70:30, denoted CA and CG, respectively, in accordance with the well-known CuZn system [38]. Both CA and CG were synthesized as a layered double hydroxide (LDH) via coprecipitation [39, 40]. Since Ga_2O_3 is not only able to form several different polymorphs [41] or an amorphous material but can also be potentially reduced and then alloyed with Cu [15], a variety of phase changes and oxidation states due to alloy formation are expected throughout transformation from the precursor state to the activated catalyst and under reaction conditions. Hence, we employ in situ and operando XAS and XRPD as complementary tools to access element-specific information on oxidation state and structure under relevant activation and reaction conditions [28–31]. This approach allows us to isolate and amplify the effects of Ga as a second component of Cu-based catalysts under reductive activation and CO_2 hydrogenation at different temperatures. With expected phase transformations and possible alloy formation, this study aims to provide an in-depth understanding of the role of Ga promotion of copper catalysts under different conditions.

2 | Experimental Section

2.1 | Catalyst Preparation

All syntheses were performed using an automated synthesis workstation (Optimax 1001, Mettler Toledo), employing computer-controlled dosing rates as well as automated heating, cooling, and stirring. The pH value was also automatically adjusted by a computer and measured using an InLab Semi-Micro-L pH electrode from Mettler Toledo, allowing for a highly reproducible synthesis.

The precursors were prepared employing a constant pH co-precipitation. In a typical synthesis, 200 mL of distilled water was cooled to 5 °C, and the pH was adjusted to 9. Afterward, 150 g of a 0.4 M aqueous solution of copper nitrate ($Cu(NO_3)_2 \cdot 3\,H_2O$, Roth) and gallium nitrate ($Ga(NO_3)_3 \cdot xH_2O$, chempur) or aluminum nitrate ($Al(NO_3)_3 \cdot 9\,H_2O$, Grüssing) was dosed under constant stirring (300 rpm) at a rate of 2.5 g/min. The pH was kept constant through the co-dosing of an aqueous base solution containing 1 M sodium hydroxide (NaOH, Grüssing) as well as 0.09 M sodium carbonate (Na_2CO_3, Grüssing), and the temperature was

kept at 5 °C. After dosing, the precipitate was aged at 5 °C under constant stirring (300 rpm) without pH control for an hour before being washed with demin. water by centrifugation until the conductivity of the washing water was below 50 µS/cm. Afterward, the product was dried in a furnace at 60 °C overnight and ground to a fine powder. To obtain the calcined samples, the precursors were heated to 600 °C with a heating rate of 2 °C/min and held at that temperature for 3 h before cooling down naturally inside the oven.

2.2 | Catalytic Activity Test

Catalytic tests were carried out with an Avantium Flowrence XD catalytic testing unit with four parallel reactors operating in fixed-bed configuration. For all catalytic measurements, quartz tube reactors with an inner diameter of 2 mm were used. The reactors were loaded with SiC to a height of 10 cm, followed by the catalyst and another layer of SiC, after which the total bed length was 23.5 cm. One reactor was loaded with SiC only and used as a reference. To reduce the catalysts, they were heated to 275 °C or 480 °C with a heating rate of 2 °C/min and held at that temperature for 4 h in a 5% H_2 in N_2 stream of 33 sccm per reactor. Afterwards, they were cooled to 230 °C before the gas feed was changed to 8.5 sccm of a 3:1 mixture of H_2 and CO_2, including 0.5 sccm He as reference gas, and the pressure was increased to 20 bar. These conditions were held for 32 h before the pressure was released, the system flushed with nitrogen, and the catalyst recovered inertly.

2.3 | Synchrotron-Based in situ and operando Characterization

In situ and operando XAS and XRPD were performed at the BALDER beamline at the MAX IV Laboratory synchrotron facility, Lund University in Sweden [42]. Gas-dosage was performed through our own self-designed high-pressure setup. A continuous flow capillary reactor (quartz, 1.5 mm outer diameter, 100 mm length, 0.05 mm wall thickness) was filled with ≈7 mg of the diluted catalyst (sieve fraction 50–100 µm, 1:6 SiO_2 dilution). The outlet gas stream was attached to a mass spectrometer (ThermoStar GSD320 T1). X-ray absorption spectra were recorded at the Cu K-edge (8979 eV) and the Ga K-edge (10367 eV) in transmission mode with a beam size of 100 × 100 µm^2 (FWHM). A liquid N_2-cooled double crystal (Si111) monochromator (FMB Oxford, UK) was used. The XRPD data were collected at 13 keV using a 2D detector (Dectris EIGER 1 M) with 1030 × 1065 pixels. For combined XAS-XRPD operando measurements, sequences composed of Cu K edge XAS, Ga K edge XAS, and XRPD at 13 keV were subsequently repeated, yielding an effective time-resolution of approx. 9 s. Pawley fits to determine the lattice parameters and domain sizes were carried out using TOPAS Academic version 6.0 [43]. We note that the reported domain sizes (D_{Vol}) are lower limits, since effects of instrumental broadening and strain were neglected for the operando data. A beam damage test was conducted prior to the experiments to evaluate the impact of the focused beam on the reduction behavior of the sample. As a result, early (low temperature) reduction of Cu was observed as a consequence of 10 min focused beam radiation. To mitigate beam-induced effects, the probed spot was changed after each of the subsequent repeats of the XAS-XRPD measurement sequence. In total, 100 unique spots were probed and subsequently repeated, such that the 101st measurement is conducted on the first spot again. Details are documented in the Supporting Information (Section 4.1). XAS/XRPD during temperature-programmed reduction (TPR) was recorded by heating the sample to 275 °C (5 °C/min, 1 h hold) in 5% H_2 in N_2 at ambient pressure. Throughout the experiment, the gas hourly space velocity (GHSV) was kept at 3 × 10^5 h^{-1}. Subsequently, a gas atmosphere consisting of H_2/CO_2 (3:1) in 12% N_2, 230 °C, and 20 bar pressure was applied. The sample was then heated to 330 °C (5 °C/min), followed by heating in 50 °C steps until 530 °C (5 °C/min). Each temperature step (280 °C, 330 °C, 380 °C, 430 °C, 480 °C, and 530 °C) was held for 30 min while XAS and XRPD were recorded. Between the different conditions, the reactor was allowed to cool to room temperature at a rate of 25 °C/min to record room temperature EXAFS. EXAFS analysis was conducted using the software Artemis from the IFEFFIT software package [44]. A table with the summarized results and details of the fitting settings can be found in the description of Table S5.

2.4 | DFT Calculations

Phase diagrams and lattice parameters were calculated by DFT using the Vienna ab initio simulation package (VASP) [45, 46] in version 5.4.1 in conjunction with the atomic simulation environment (ASE) [47]. The projector augmented wave (PAW) [48, 49] method and the Bayesian Error Estimation Functional with van der Waals correlations (BEEF-vdW) [50] exchange-correlation functional were employed. The plane wave cutoff energy was 500 eV in all calculations. All bulk structures were taken from the MaterialsProject database [51] Monkhorst-Pack k-point sampling [52] and detailed unit cell parameters are given in the Supporting Information (Section 5.2). The geometries of all structures have been optimized until the forces were less than 0.01 eV/Å. The vibrational analysis for the gas phase species H_2 and H_2O was performed using the finite difference method in the harmonic approximation with a resolution of 0.01 Å. Phase diagrams are constructed as a function of temperature and H_2O/H_2 ratio, using bulk β-Ga_2O_3, H_2 and H_2O in the gas phase as reference systems. Entropy contributions from the solid phases (metal, alloys, and oxide) were not considered.

3 | Results and Discussion

3.1 | Precursors

To ensure that the desired crystalline precursor phase was achieved, laboratory XRPD was applied. The XRPD patterns (Figure 1a) show that both materials crystallized as layered double hydroxides. Since no additionally reflections are present, it can be assumed that the samples do not contain crystalline byphases. The broader reflections exhibited by CA compared to CG indicate that smaller coherently scattering domains are present in CA. While the *00l* reflections are only slightly more broadened for CA, the other reflections (mostly cross-plane reflections, e.g., 13-1) seem much more broadened, hinting at stacking faults. SEM images (Figure 1b,e) show that CG (Figure 1b) and CA (Figure 1c)

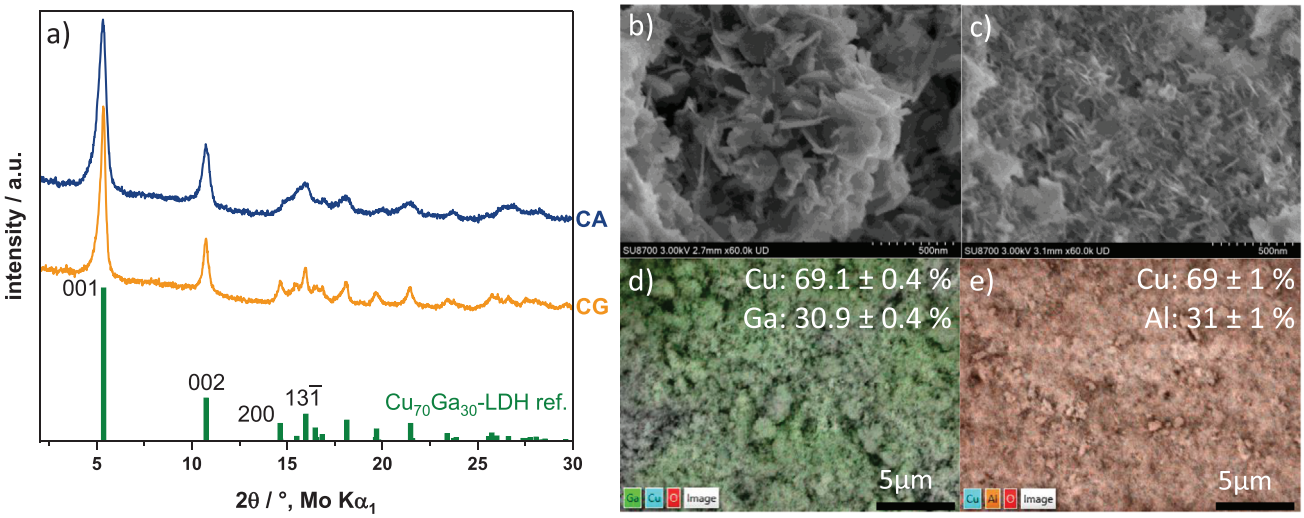

FIGURE 1 | XRPD-patterns (a) of CA (blue), CG (orange), as well as a calculated reference for a CuGa-LDH, which was refined using a CuAl-LDH reference [53], as well as SEM images of CG (b) and CA (c). Additionally, the results of elemental mapping of CG (d) and CA (e) are shown as an overlay, indicating homogenous distribution of the elements Cu (turquoise) and oxygen (red) with either gallium (lime) or aluminum (orange) within the precursors and confirming that the target Cu:M (M = Ga, Al) ratio of 70:30 was achieved.

both exhibit platelet-like shape particles. While CA forms rather small platelets of around 150 nm diameter and a thickness of roughly 20 nm, which are strongly intergrown, CG consists of larger, thicker and less intergrown platelets with a diameter of approximately 350 nm and a thickness of around 50 nm. EDX mappings (Figure 1d,e) revealed that Cu, O, and M (M = Ga, Al) are homogenously distributed throughout the sample on the micrometer scale. Additionally, the difference in particle size might be one reason for the larger surface area of CA of 71 m^2/g in comparison to CG with 45 m^2/g, which was determined by N_2 physisorption using the BET method. In both cases, a type H3 hysteresis loop is present, which is typical for platelet-like particles and indicates textural porosity (Figure S1). Furthermore, the smaller hysteresis loop in CG suggests less textural porosity, which is likely due to the bigger platelets and also explains the smaller surface area of CG.

Regarding the chemical composition of the material, ICP-OES measurements (Table S2) and EDX mappings (Figure 1d,e) confirmed that the targeted molar Cu:M (M = Al, Ga) ratio of 70:30 was achieved within the error margin, although the Cu:Ga ratio determined by ICP was slightly higher, suggesting a Cu:Ga ratio of 73:27 ± 2. Based on these results as well as thermogravimetric analysis (Figure S2) and elemental analysis (Table S1) the sum formulas for CG ($Cu_{14}Ga_6(OH)_{40}(CO_3)_3 \cdot 12\ H_2O$) as well as for CA ($Cu_{14}Al_6(OH)_{40}(CO_3)_3 \cdot 10\ H_2O$) were determined.

Additionally, the reduction behavior of calcined and uncalcined CG was measured by H_2TPR (Figure S4). While the uncalcined sample exhibited only one reduction event, at least three reduction events were present for the calcined sample. This is likely due to different sources of reducible copper in the calcined sample, e.g., by the formation of CuO (Figure S3) and probably amorphous $CuGa_2O_4$. Since this would increase the complexity of the system and hinder the interpretation of catalytic activity data, the precursors were directly reduced without a calcination step in between (Figure 2a). Therefore, all results discussed hereafter are based on directly reduced precursors, which were not calcined prior to reduction.

The main reduction event for uncalcined CG and CA consists in both cases of a shoulder starting at around 150 °C, which is followed by a sharp peak with a maximum at approximately 275 °C. This could either be interpreted as two different reducible copper species with similar reduction temperatures or as the stepwise reduction of $Cu^{2+} \rightarrow Cu^{+} \rightarrow Cu^{0}$, with the latter being significantly more likely not only due to the fact that a single source precursor was used but also because the areas of the shoulder and the main peak are rather similar for both systems, which is a strong hint at a stepwise reduction of a single Cu^{2+}-species [54–56]. Regarding the shape of the shoulders, there is a clear difference between CA and CG. While the shoulder during the reduction of CA starts slowly at first and increases sharply afterwards, in the case of CG, an almost linear increase in H_2-consumption was observed. This might indicate that Ga-species could potentially facilitate the reduction of Cu^{2+}, explaining the steeper increase at the start and stabilizing Cu^{+}, which would explain the lack of a rising H_2-consumption as observed for CA. Furthermore, an additional reduction event starting around 400 °C is present for CG, indicating reduction of Ga-species and formation of an alloy with Cu. Assuming complete reduction of Cu, roughly 50% of Ga^{3+} was reduced to Ga^0 according to the ongoing H_2 consumption over the course of the TPR experiment up to 550 °C. The formation of a Cu_xGa_y alloy was proven by TPR experiments aborted at 530 °C with a holding time of 0 and 4 h and subsequent XRPD measurements (Figure 2b), which exhibits a shift toward lower q. A magnification of this can be found in the Supporting Information (Figure S7). Since the alloying was progressing notably further in the sample held for 4 h at 530 °C compared to the one without holding time, it can be concluded that the Ga reduction and alloying with Cu does evolve slowly at this temperature.

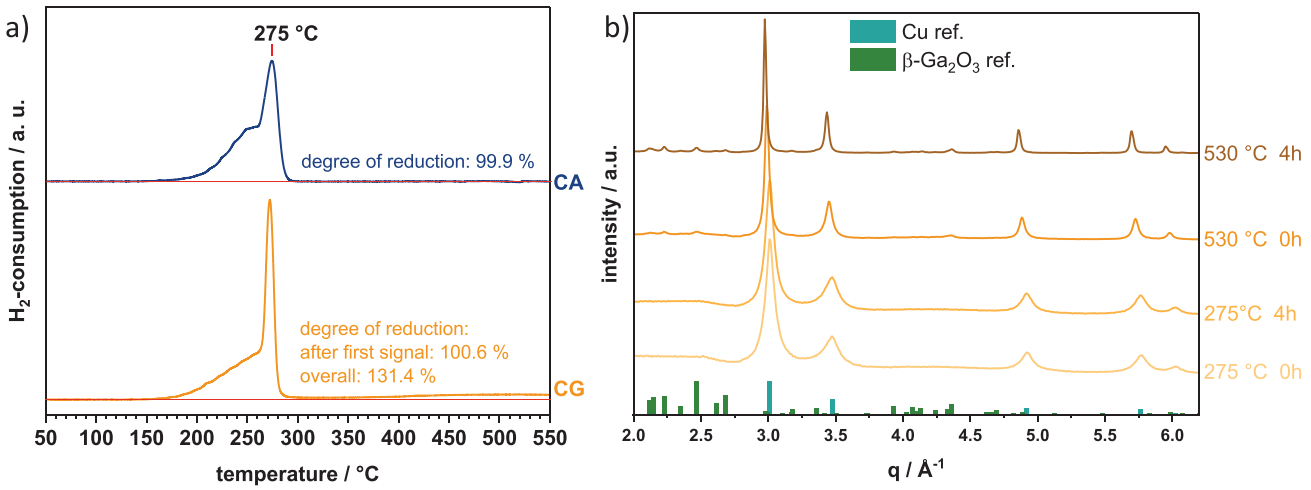

FIGURE 2 | (a) TPR measurements of CG and CA. Both samples exhibit their main reduction event at roughly 275 °C, with CG also showing an additional reduction event after around 400 °C. In both cases, the baseline is given to highlight the additional reduction step in CG and the lack thereof in CA. The degree of reduction was calculated based on the amount of Cu^{2+} in the sample, suggesting complete reduction of Cu^{2+} to Cu^0 in the case of CA and additional reduction of Ga^{3+} in the case of CG. (b) XRPD measurements of CG after TPR at 275 °C and 530 °C with a holding time of either 0 h or 4 h at the respective temperature. All depicted XRPDs were recorded at room temperature. Additionally, calculated peak positions and intensities of Cu [57] (turquoise) and β-Ga_2O_3 [58] (green) are shown.

In summary, the two catalysts CA and CG show a strong similarity regarding their Cu content, XRPD patterns, particle morphology and TPR peak maximum, while differences can be found in the XRPD peak shapes, the particle size and detailed TPR profiles. The most striking difference seems to be the possibility of partial support reduction and alloy formation in case of CG, but not CA. While the bulk reduction shows an onset near 400 °C, which is beyond the reduction or reaction temperatures of typical Cu-based methanol synthesis catalysts, the driving force toward bulk alloying renders the presence of reduced surface species similar to the famous Cu-Zn SMSI [59] possible in this system.

3.2 | Catalytic Activity

In order to compare the catalytic activity of CG and CA, we performed stability tests for both catalysts (Figures S9-S11). After an initial formation period, only slight deactivation occurred for CG, while no deactivation was present for CA and we used this steady state region for the comparison. Reduction of the precursors were performed at 275 °C and 480 °C to produce not only a Cu/M_2O_3 (M = Al, Ga) catalyst, but in case of CG also a Cu_xGa_y/Ga_2O_3 catalyst to probe how formation of the alloy affects the catalytic activity or selectivity. Precursors reduced at 275 °C or 480 °C are additionally labeled with the reduction temperature, resulting in e.g. CG_275 for CG reduced at 275 °C. As can be seen in Figure 3, in case of CA_275, a CO_2-conversion of roughly 9% and a MeOH formation rate of 0.7 mmol g_{Cu}^{-1} h^{-1} were found, which only decreased slightly to 8% for CA_480 with the MeOH formation rate remaining unchanged, suggesting good thermal stability of the CA-systems. On the other hand, CG_275 exhibits CO_2-conversion of only 2% (1/4 of that of CA_275). The MeOH formation rate of CG_275 was found to be 0.3 mmol g_{Cu}^{-1} h^{-1}, which is nearly half that of CA_275. This demonstrates that Ga-species in the catalyst have a promoting effect on the selectivity but due to the lower overall CO_2-conversion the total MeOH yield of CG_275 is also lower. For CG_480, the CO_2-conversion was only a quarter compared to CG_275 and hardly any MeOH was detected, resulting in a decrease of MeOH formation rate by a factor of roughly 1/33. While the decrease in CO_2-conversion can be explained by strong sintering (Figure S12) during the alloying of Cu with reduced Ga which is discussed later, the poor MeOH formation rate cannot. While Kordus et al. [17] reported a promoting effect of alloying Cu with small amounts of Ga (0.3 atomic % Ga), our study suggests a

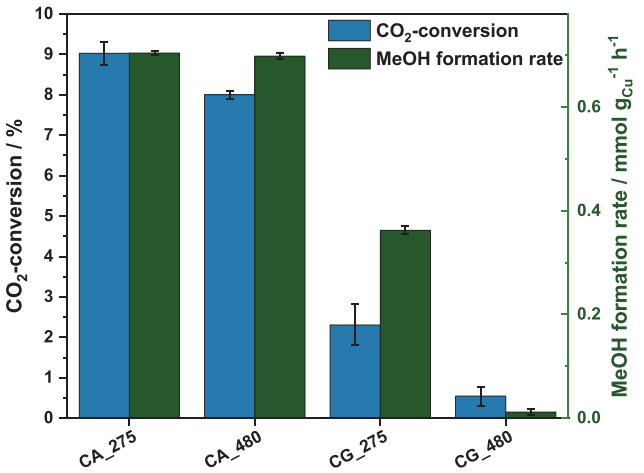

FIGURE 3 | CO_2-conversion and MeOH formation rate as well as the standard deviation of CA_275, CA_480, CG_275, and CG_480 after 7 h on stream. To calculate the standard deviation, values between 6 and 10 h on stream were used. Using a reduction temperature of 480 °C reduces the conversion in both cases, but does not influence the MeOH formation rate in the case of CA_480. For CG_480, however, barely any MeOH is detectable at steady state conditions (230 °C, 8.5 sccm H_2/CO_2 3:1, including 0.5 sccm He, 20 bar).

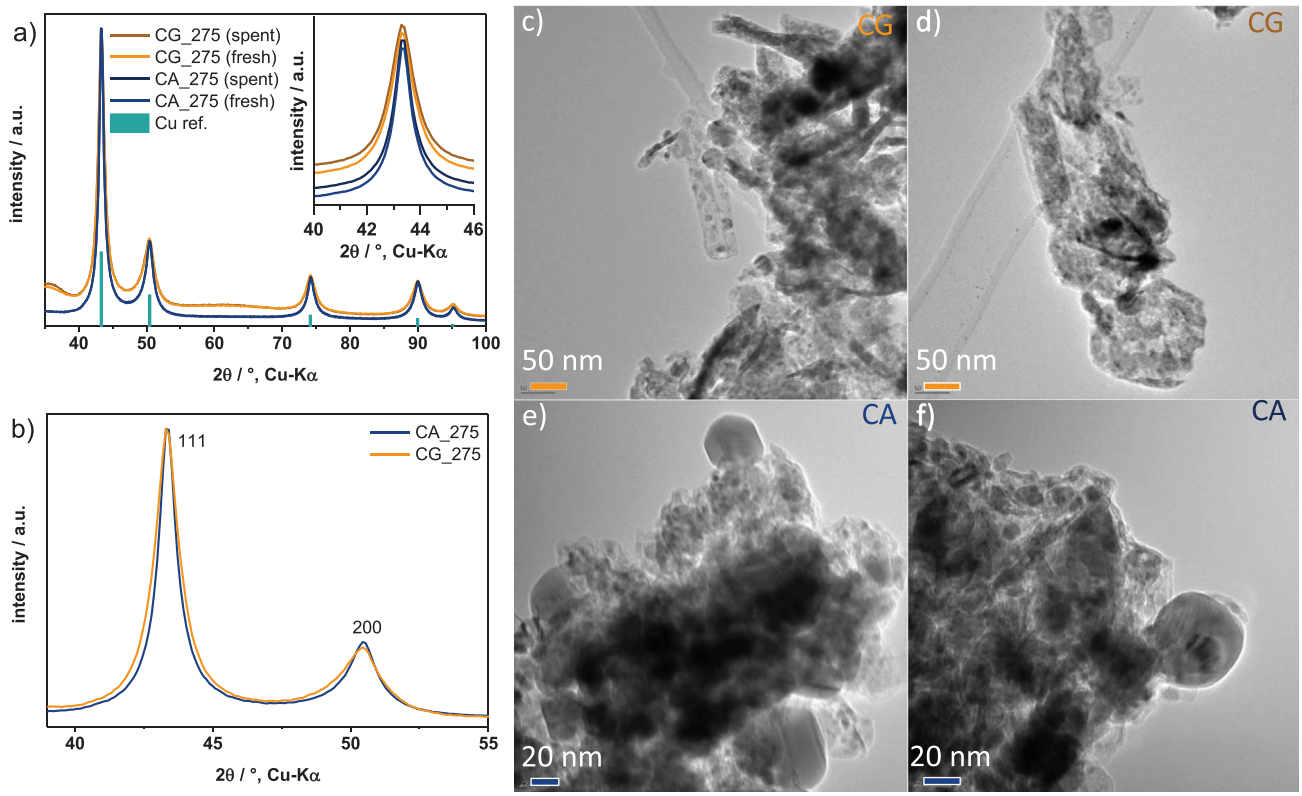

FIGURE 4 | (a) Normalized XRPD-patterns of CG_275 (orange) and CA_275 (blue) directly after reduction (lighter color) as well as after 32 h on stream (darker color). In the inset, the patterns are vertically offset to resolve the overlap in the main panel. Additionally, calculated peak positions and intensities of Cu (turquoise) are shown [57]. (b) Scaled patterns of the CG_275 and CA_275 to highlight the difference in the line shape, i.e., a slightly stronger broadening of the (111)-reflection for CG_275 and additional peak asymmetry for the 200-reflection for CG_275, indicative of a higher density of planar defects. (c–f) TEM images of freshly reduced CG_275 (c) and spent CG_275 (d), as well as freshly reduced CA_275 (e) and spent CA_275 (f) with a time on stream of 32 h for both spent catalysts. In the case of CG, a lower magnification had to be used due to electrostatic effects from the sample.

negative effect if the fraction of Ga is too high. After the stability test, the samples were characterized without exposure to air by laboratory XRPD (Figures 4a,b and S12) and TEM (Figure 4c–f) to investigate changes in their composition and structure. No Bragg peaks for crystalline M_2O_3 phases could be observed neither in fresh nor spent CA_275 and CG_275. Through Pawley fits of the metallic Cu phase, which is being present in the fcc structure, the domain sizes of the freshly reduced and spent samples (ToS = 32 h) were determined. In both cases, the domain size of freshly reduced CG_275 (5.23 ± 0.07 nm) and CA_275 (6.56 ± 0.08 nm) does not differ within the error margins from spent CG_275 (5.17 ± 0.07 nm) and CA_275 (6.44 ± 0.08 nm), suggesting that both catalysts do not sinter. The lattice parameter is also identical within the error margins for all four samples (3.616 Å), indicating no measurable alloy formation of CG_275 in the bulk in agreement with the alloying onset at higher temperatures determined by TPR and XAS. Thus, the observed deactivation during the formation period cannot be linked to sintering or changes in the bulk of Cu. Furthermore, there are slight but yet evident differences in the lineshape of the Cu phase between CG_275 and CA_275 (cf. Figure 4b): The former shows a broader 111-reflection and in particular a more pronounced asymmetry of the 200-reflection. The latter indicates a higher density of planar defects (in particular stacking faults) for the Cu in CG_275 [60]. Thus, the smaller apparent domain size is likely due to a higher concentration of defects besides slightly smaller domains in the crystallites. A correlation between such defects and catalytic activity in methanol synthesis has been proposed [18], but the synthetic factor to control this properties is not clear. However, for our two samples it correlates inversely with the size of the precursor crystallites, but may also originate from slight differences observed in the reduction behavior on the different support materials or in different reactors (c.f. lab based TPR and operando XAS during TPR, vide infra).

The domain size (6.77 ± 0.08 nm) of spent CA_480 differs only slightly from freshly reduced CA_275 (6.56 ± 0.08 nm), indicating that barely any sintering took place. In case of spent CG_480 however, the domain size (12.1 ± 0.2 nm) increased significantly compared to the freshly reduced sample (5.23 ± 0.07 nm), indicating strong sintering. Additionally, the lattice parameter (3.653 Å) increased substantially, proving the formation of a Cu_xGa_y bulk alloy (Figure S12).

Besides the average domain size also the size distribution and dispersion of Cu on the amorphous oxide support is of interest, which was studied with TEM measurements (Figure 4c–f). These revealed that in both fresh and spent state most copper particles in CA_275 range from a few nanometer up to around 10 nm, with some exceptions reaching roughly 40 nm. Thus, no indication for significant sintering was found, which is in line with the XRPD results. For CG_275, Cu particles of around 20–40 nm

were found, but there were also many rather small particles, which are most likely also Cu, due to their contrast in TEM and their well-defined spherical form. Again, the characteristics of the spent CG_275 catalyst are nearly identical, rendering sintering an unlikely reason for the observed initial deactivation under reaction conditions (Figure S9).

In summary, despite the similarities between CA_275 and CG_275, particularly with regard to the unalloyed bulk properties of the Cu phase, their similar average particle sizes and sintering stability, marked differences have been observed in their catalytic behavior. While a positive effect of the Ga_2O_3 support on the methanol selectivity was observed, the activity of this catalyst was rather low and unstable. At the relevant reduction and reaction temperature for methanol synthesis, no bulk-alloying was observed that could explain these differences calling for in situ and operando experiments to capture the dynamic behavior of the Ga_2O_3 support during reduction and reaction.

3.3 | In situ and operando Experiments

In order to monitor both the short- and long-range order structure of the CA and CG systems during catalyst activation, reaction, and temperature increase, operando XAS and XRPD measurements were combined in the same experiment. At first, activation of the as-prepared catalysts was investigated, revealing the reduction of Cu^{2+} to Cu^0 by heating the reactor to 275 °C (5 °C/min) in 5% H_2/N_2 with a GHSV of the total flow of $3 \times 10^5\ h^{-1}$. According to a linear combination analysis (Figure S14), Cu was reduced gradually in both samples from Cu^{2+} over Cu^+ to Cu^0, as it was also seen by the shoulders in the TPR profiles during lab experiments. The formation of Cu^+ is more pronounced for CG, as proposed in H_2-TPR. The Fourier transformed (FT) EXAFS spectra (not corrected for phase shift) of both CA and CG at the Cu K-edge depicted in Figure 5d,e show no signal originating from Cu-O scattering (1.5 Å) but increased intensity for metal-metal scattering (2.2 Å), indicating that Cu is fully reduced to the metallic state in both catalysts after TPR up to 275 °C in line with the H_2-consumption in the lab-TPR. Interestingly, the TPR also impacts the state of Ga, as changes in the XANES at the Ga K edge become visible (Figure 5c).

XANES, however, is not only sensitive with regard to the oxidation state, but also provides information on coordination geometry [61]. Hence, the changes in the XANES at the Ga K edge can be predominantly influenced by the change of the local coordination environment of Ga during phase transitions. Hereby, Ga does not change simultaneously with the stepwise reduction of Cu ($Cu^{2+} \rightarrow Cu^+ \rightarrow Cu^0$) as the transition of the Ga species starts before the occurrence of metallic Cu (Figures S14 and S15), which makes it unlikely to relate it to co-reduction. However, along with other reports [15, 18], we cannot exclude Ga^0 formation to a small extent at this point. Comparison with references suggests that the majority of the Ga^{3+} is still primarily positioned in octahedral coordination after TPR, which will be further addressed later. The edge energy of the initial state of CG, meaning the LDH precursor, is located at 10373 eV (Table S5), which cannot be related to the Ga_2O_3 polymorphs used as references, while the shape of the XANES is reminiscent of that of commercial Ga_2O_3.

3.3.1 | operando XAS and XRPD During the CO_2-to-Methanol Reaction

After TPR, reaction conditions were applied (230 °C, 90% H_2/CO_2 3:1 and 10% N_2, GHSV 30,000 h^{-1}, 20 bar) and held for 1 h. Methanol formation was detected by mass spectrometry (Figure S16). No changes were observed in the XANES and EXAFS at the Cu K edge of CA or CG during switching from reduction to the feed. The Ga K edge XANES/EXAFS also remained similar (Figures 5 and S16).

Next, the temperature was increased to 280, 330, 380, 430, 480, and 530 °C (5 °C/min) with 30 min holding time, respectively. The aim of the temperature rise was to mimic hot-spot formations and to accelerate aging phenomena of the catalysts. operando synchrotron XRPD allowed to monitor the evolution of the lattice parameter and domain size for the metallic Cu. For Cu in CA, a roughly linear thermal expansion was detected (Figure 6a). The cell parameter a for Cu in CG in the Figure 6a follows that of Cu in CA up to 430 °C. However, a sudden increase was observed at 480 °C and 530 °C, strongly indicating bulk alloy formation between Cu and Ga. This is consistent with the ex situ experiments from TPR. The crystalline domain size (Figure 6c) increased almost linearly with temperature for CA, while for CG significantly larger domain sizes were observed starting from 380 °C, indicating the onset of faster sintering. This indicates an increased mobility of copper over the Ga_2O_3 support likely connected to the onset of Ga mobility in the underlying support triggered by formation of a bulk alloy at 480 °C. Crystallization of β-Ga_2O_3 was observed during temperature dwelling at 530 °C (first and last scans at this temperature shown in Figure 6d), while Al_2O_3 remains amorphous throughout the entire experiment. Note that with XRPD the analysis is limited to crystalline phases, while further insights are possible when analyzing the simultaneously acquired XAS data. The FT-EXAFS at the Cu K-edge reveals an increased amplitude of the Cu–Cu scattering signal between 1.6 and 2.7 Å (Figure 5d,e), which indicates sintering to larger particles at elevated temperatures [62, 63]. Also, fits of the EXAFS data using Cu foil as a reference showed that the coordination number (CN) increased from 9.5 to 10.7 and from 8.7 to 9.0 after TPR for CA and CG, respectively. We note, that an incorporation of Ga in the Cu structure can lead to a lower backscattering contribution in the FT-EXAFS (Cu–Cu first shell). This effect was supported with calculated FT EXAFS of a Cu and a Cu_9Ga_4 structure provided in Figure S19. Thus, the resulting lower amplitude observed for the CG EXAFS gives rise to a lower CN when fitting the FT spectra. There are additional explanations for the apparent divergence between the larger domain sizes deduced from XRPD for CG and the higher Cu–Cu coordination numbers obtained by EXAFS for CA. This opposition can be reconciled by considering the distinct structural effects of the two supports. In CG, the more dynamic crystallizing Ga_2O_3 favors the merging of coherent Cu domains, which are readily detected by XRPD. At the same time, partial reduction and beginning alloying leads to substitution of first-shell Cu neighbors by Ga atom, together with lattice defects/distortion introduced during alloying/dealloying, may lower the average Cu–Cu coordination number recorded by EXAFS. Both Cu and Ga are similar but not the same backscatters, which leads to a distortion. This distortion results in increasing effective Cu–Cu distances with incorporation of Ga and is demonstrated through

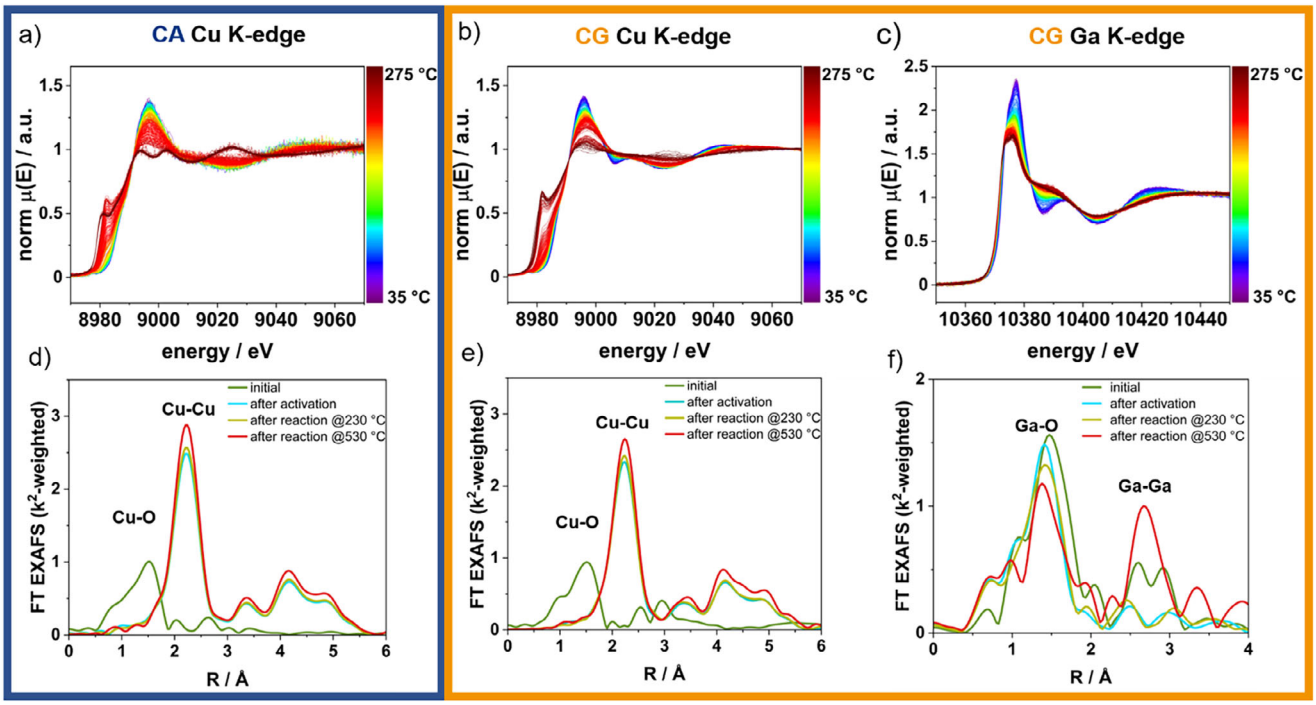

FIGURE 5 | (a–c) XANES during TPR to 275 °C of CA (a) and CG (b) at the Cu K edge and at the Ga K edge (c) for CG; (d–f) Fourier-transformed EXAFS spectra of CA and CG at the (d, e) Cu K edge and (f) Ga K edge at different stages of the experimental procedure.

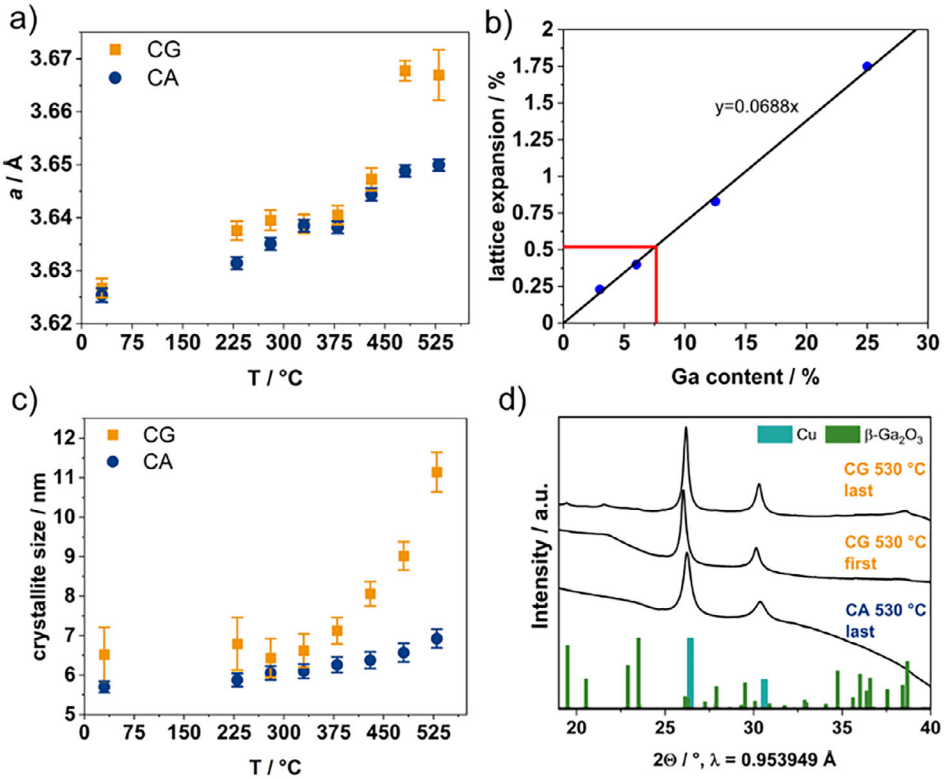

FIGURE 6 | Operando XRPD during CO_2 hydrogenation to methanol: (a) Cell parameter and (b) calculated lattice expansion of various Cu-Ga alloys with fcc structure as a function of the Ga content, including $Cu_{31}Ga$, $Cu_{15}Ga$, Cu_7Ga, and Cu_3Ga. The red line indicates the percentage of lattice expansion and estimated Ga content found in the experiments during TPR at 480 °C. (c) Domain sizes of CA and CG. Error bars are derived from the variation of all data points collected at each temperature. (d) Selected XRPD patterns, evidencing the crystallization of β-Ga_2O_3 upon prolonged dwelling at 530 °C.

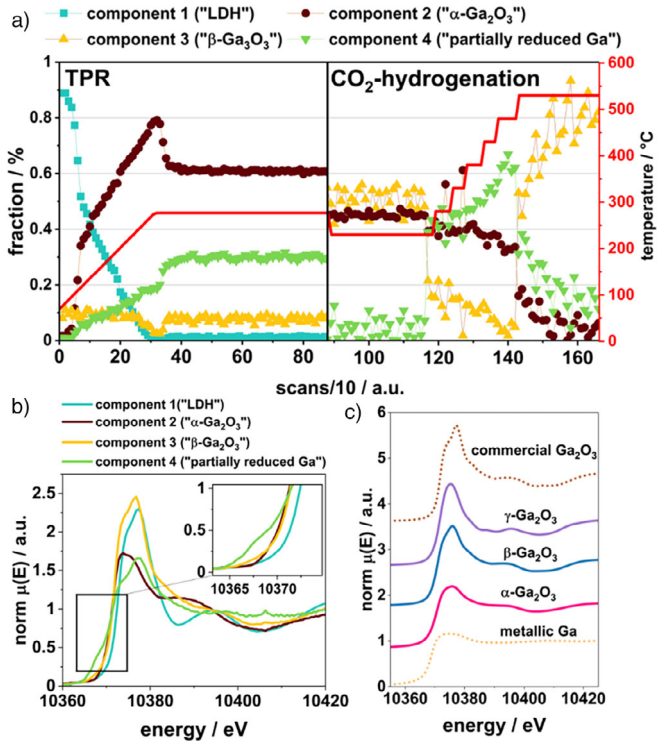

FIGURE 7 | (a) Fractions of components along the experiment as a result of multivariate curve resolution-alternating least square (MCR-ALS) analysis of XANES at the Ga K edge during TPR and under reaction condition. (b) XANES spectra of components derived by MCR-ALS. (c) Reference spectra for Ga-oxides and metallic Ga resembling the components in Figure 7b.

theoretical structure models listed in Table S8. In CA, Al cannot be incorporated into the copper particles leading to a stable and well-ordered environment of Cu neighbors and thus a higher Cu–Cu coordination number. To further quantify the structural changes revealed for Ga during TPR and in CO_2 hydrogenation conditions, multivariate curve resolution with alternating least squares algorithm (MCR-ALS) analysis was used (Figure 7). This technique is typically employed to decompose complex, overlapping spectral data into spectra of pure components and their concentration profiles. It works iteratively by alternating between estimating concentration and spectral profiles using least squares, leading to identification and quantification of components in mixtures without the need for prior knowledge of pure spectra [64]. MCR-ALS revealed that the XANES spectra set at the Ga K edge of CG consisted of four components; the corresponding spectra are shown in Figure 7b, whereas the temporal evolution of the compounds during the experiment is shown in Figure 7a. Component 1 represents the initial state of the catalyst, in which Ga^{3+} is part of the layered double-hydroxide (LDH) structure, surrounded by hydroxide ions. Upon TPR, this initial state of the catalyst transforms into three different components (Figure 7a), named components 2, 3 and 4 in Figure 7b. When comparing the MCR-extracted spectra with reference spectra (Figure 7c), which were taken from literature [65], similarities between the two sets of spectra become apparent. With a rather flat main absorption feature, component 2 shows similarities to α-Ga_2O_3, a corundum structure with Ga^{3+} situated in the octahedral positions [61]. As α-Ga_2O_3 and Ga^0 both show a similar shape of the plateau-like absorption feature (Figure 7c), MCR-ALS has to be regarded with caution. The energies of the absorption edges and the pre-edge region furthermore helps to distinguish between the Ga species when present simultaneously. A table with the absorption edges of samples and references is given in Table S5. Meanwhile component 3 can be identified as a Ga_2O_3 like structure, in which Ga occupies statistically both tetrahedral and octahedral positions, as the calculated spectrum resembles β- and γ-Ga_2O_3 [66]. Linear combination analysis (LCA) of component 3 revealed that the spectrum is more similar to β-Ga_2O_3 than to γ-Ga_2O_3, which is in line with XRPD results showing crystallization of β-Ga_2O_3 at higher temperatures. The fourth isolated spectrum shows a pre-edge feature at 10368 eV (Figure 7b). This pre-edge feature originates from reduced Ga (Figure 7c, Table S5). As the extracted spectrum "component 4" does not fully resemble the spectrum for metallic Ga, we assume that only a fraction of the Ga-species was reduced to Ga^0. Partially reduced Ga has been reported in a similar case, in which a CuGa catalyst was reduced in H_2 at >400 °C [17]. In the study by Kordus et al. [17], the shoulder in the pre-edge region of the Ga XANES was used for identification of partially reduced Ga due to the presence of a Cu_xGa_y alloy. Notably, the MCR-extracted spectra do not fully represent one or another reference Ga phase in particular, but could be composed of Ga species not represented within the set of reference spectra. This also applies to the extracted spectrum of component 4, in which parts of the spectrum's features can be traced back to reduced Ga while the majority is still similar to the spectra of Ga-oxides. The amount of Ga reference spectra was limited to the set shown in Figure 7c and a quantification of dedicated Ga species and phases is therefore not possible. More importantly, the dynamics of Ga in this catalyst can be easily monitored with MCR-ALS.

Together with the XRPD results, this transformation during TPR seen in the MCR-ALS results can be explained by the thermal decomposition of the crystalline LDH precursor (assigned to component 1) toward amorphous Ga_2O_3 support with a short-range ordering mainly resembling α-Ga_2O_3. This observation is similar to the thermal behavior of amorphous $Ga(OH)_3$ gel reported in literature, which transforms into poorly crystalline γ-Ga_2O_3 in this temperature range [67]. In the study by Li et al. [66] and in agreement with the known thermal instability of γ-Ga_2O_3, further heating leads to crystallization of the thermodynamically stable β-Ga_2O_3 polymorph at even higher temperatures. The crystallization of β-Ga_2O_3 is also observed toward the end of our experiment. Simultaneously with the decomposition of the LDH (component 1), a Ga-phase named component 4 was formed during TPR to an extent of about 30%. Prominent in component 4 is the pre-edge shoulder, which can be traced back to partially reduced Ga. Notably, this shoulder is not significantly evolved in the XANES pre-edge region during TPR (Table S5), indicating the absence of bulk-reduced Ga at this point. As component 1 represents the LDH structure, which was irreversibly decomposed, the MCR-ALS analysis of the spectra after TPR was performed with only the remaining 3 components. Switching to reaction conditions (230 °C, H_2/CO_2 3:1 in 10% N_2, GHSV 3 × 10^5 h^{-1}, 20 bar) resulted in the decrease of component 4, while the β-Ga_2O_3 (component 3) is now formed to an extent of almost 50%. This phase diminishes once the temperature is increased to 280 °C. It is noted that the drop in the amount of component 3 in Figure 7a under reaction conditions at 280 °C could have been

affected by the cool-down of the catalyst, which was performed for increased spectra quality and for better comparability of the EXAFS. Simultaneously with increasing temperatures under reaction conditions, the content of α-Ga_2O_3 (component 2) decreases, and the fraction of component 4 increases. This time, a clear shift in the pre-edge feature of the XANES at the Ga K-edge is observed (Figure S18), indicating the progressive reduction of Ga at higher temperatures. This correlates with the increase in component 4, which peaks at approximately 65% at 480 °C. At this stage, the spectral features related to reduced Ga and the sudden change in the cell parameters (Figure 6) suggest the formation of a Cu_xGa_y alloy in which Ga is in the oxidation state 0. At a higher temperature of 530 °C, the XANES features change markedly, with the pre-edge feature previously developed significantly diminished (Figure S18). The concentration of component 4 then accordingly decreased to approximately 20% of the Ga species. For the formed Cu_xGa_y alloy, this would correspond to around 6% of Ga in the Cu particles. In parallel, the MCR-ALS analysis suggests a pronounced formation of component 3, which we found to be best represented by β-Ga_2O_3.

After cooling back to room temperature, comparison of the Fourier transformed EXAFS of CG at the Ga K edge (Figure 5f) reveals strong differences between the spectra recorded in the initial state, after activation, after reaction at 230 °C as well as 530 °C. The raw data are shown in Figure S21. In all spectra as well as for the reference Ga_2O_3, the Ga-O scattering (<2 Å) results in the signal with the highest intensity. For the initial state of the CG catalyst, the signal referring to the Ga-backscattering (2.5–3.5 Å) is present, but to a much lower extent than for the Ga-oxide reference. This can be explained by the fact that the uncalcined starting material is still in the layered LDH structure. Here, only those Ga atoms in the same layer are available as backscatterers in the second shell, whereas in the 3D bulk Ga_2O_3, all surrounding Ga atoms serve as backscatterers. Interestingly, the signal of Ga-backscattering is also hardly visible for the sample after the activation step, while Cu^{2+} is reduced to metallic Cu (resulting in strong Cu-backscattering in the FT EXAFS at the Cu K edge) and most of the volatile species have been removed. Hence, reduced Cu particles are formed during activation along with amorphous Ga_2O_3, in which mostly oxygen is seen (backscattering similar to Ga_2O_3). Due to the shorter Ga-O distance in Ga_2O_3, the oxygen backscattering-peak is shifted to slightly lower distances. A small contribution can be found at 2.5 Å (not corrected for phase shift), which could be attributed to Ga-M (M = Cu, Ga) interactions. This status is preserved throughout the reaction at 230 °C. The FT EXAFS at the Ga K edge after the temperature ramping in reaction atmosphere shows more prominent Ga-M backscattering appearing at 2.3 Å and 3.4 Å that have not been present in the previously recorded FT EXAFS nor the Ga-oxide reference. Models based on pure Ga oxide and Cu_xGa_y alloy fractions were used to fit the EXAFS data (Table S8), considering Ga-O and Ga-Ga or/and Ga-Cu scattering. Alongside statistical inspection provided in the Supporting Information (Table S9), we conclude that the implementation of Ga-Cu scattering alongside Ga–O and Ga–Ga scattering as most beneficial for representing the experimental EXAFS data, especially at the named feature at 2.3 Å in the phase uncorrected FT EXAFS (Figure S23). The fitting results show that after temperature ramping with Cu_xGa_y alloy formation, some of this alloy remained to a low degree even after 530 °C and cool-down, which is in line with MCR-ALS results.

In summary, the in situ and operando XAS and XRPD experiments show the trend to alloying of the CG catalyst at high temperatures. Specifically, the Cu_xGa_y alloying, followed by β-Ga_2O_3 formation under reaction conditions, indicates a combined redox and polymorph flexibility absent in the Al-containing system. Most importantly, also evidence for dynamic behavior of the Ga support at lower temperature relevant for methanol synthesis was observed mainly in the analysis of subtle changes in the XANES at the Ga K edge, which was not captured in the previous ex situ experiments [20]. Although bulk-sensitive x-ray techniques such as XAS and XRPD may miss Ga surface species or surface alloys present only in the topmost layers, the combination of element-specific operando XAS and temperature-resolved XRPD still provided interesting insight into the dynamics of Ga with possible relevance to the catalytic function. The ensemble of operando data and its comparisons to reference and to the static CA catalyst, in particular the hidden nature of the Ga dynamics at relevant low temperatures and the absence of the clear features in bulk-sensitive ex situ analytics strongly suggests that for a coherent picture of Ga's role in enhancing methanol selectivity, the surface must be considered as the effect might be limited to the near-surface region. Such possible dynamic structural transformations at the surface could be further elucidated by surface-sensitive (XPS/LEIS) and microscopic (in situ TEM) methods, complementary to the in situ and operando studies reported here. We shed further light by DFT calculations below.

3.4 | DFT Results

We calculated the lattice expansion for various Cu–Ga alloys with fcc structure up to a Ga-content of 25% and confirmed that there is a linear relationship between the Ga content and the corresponding lattice expansion (Figure 6b). From this, we estimate that the observed lattice expansion during the operando experiments at 480 °C of the Cu/Ga system of 0.52% corresponds to a Ga content of roughly 7.6% (red line in Figure 6b), such that a reduction of Ga_2O_3 and alloying to bulk Cu_xGa_y starts at these reaction conditions.

Figure 8 shows the calculated phase diagrams where the stability of bulk (Figure 8a) and surface alloys (Figure 8b) is given as a function of temperature and H_2O/H_2 ratio. The H_2O/H_2 ratio, recognized as a key thermodynamic factor, has been successfully employed to draw conclusions about phase stability in catalysts during various reactions, including the Fischer–Tropsch synthesis [68]. The estimated values for our experimental conditions for methanol synthesis (in terms of H_2O/H_2 ratios that are related to CO_2 conversion, cf. Figure 4) are indicated in the figure. We note that the reference for the gallium oxide has been set to bulk β-Ga_2O_3, which we see as an upper limit for the mostly amorphous Ga_2O_3 observed in the samples (with the exception at the highest temperature applied, 530 °C), as this would be the most stable reference component. For the bulk, the results are in very good agreement with the experimental observations that a low-Ga alloy can be formed, but only at high-temperature conditions irrelevant for typical methanol synthesis over Cu-based catalysts, i.e., 480 °C in the feed or 530 °C in the TPR. However, we estimate, based on a comparison of the phase diagrams in Figure 8, that there is already the onset of surface alloy formation under reaction conditions relevant for methanol synthesis, possibly affecting the

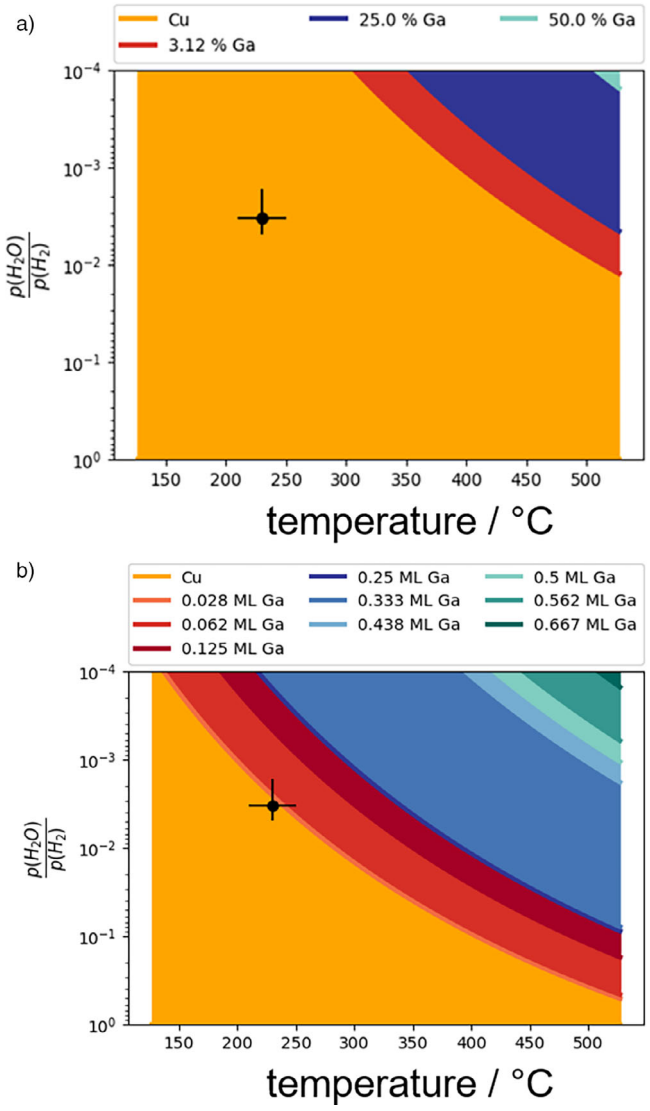

FIGURE 8 | Calculated phase diagrams of (a) bulk and (b) surface Cu_xGa_y alloys with various amounts of Ga as a function of the H_2O/H_2 pressure ratio and temperature. The calculations in (b) show the results for the Cu(111) surface, other surfaces are given in the Supporting Information. The data point refers to our experimental conditions with typical deviations marked as error bars. The phase diagrams are calculated relative to bulk Ga_2O_3.

catalytic properties in the absence of clear bulk effects as observed experimentally. We note, however, that since the hydrogenation of CO_2 produces water alongside methanol, the H_2O/H_2 ratio changes with increasing conversion [69]. This means that the degree of surface alloy formation is strongly dependent on the degree of CO_2 conversion to methanol and water in a similar way as Co is oxidized to CoO at high conversion of CO during the Fischer–Tropsch reaction [68]. In our experiments (CG_275_iso_red, Figure 4), the conversion of CO_2 to methanol is roughly 2%, corresponding to a H_2O/H_2 ratio of 3×10^{-3}.

3.5 | Discussion: Dynamics of Ga in Comparison to Al and Zn in Cu-Catalysts for Methanol Synthesis

Since Al_2O_3 is known to be a non-reducible and non-dynamic support, the comparison of catalysts with Al_2O_3 support with more dynamic support materials like Ga_2O_3 or ZnO can be very favorable. By doing so, effects based on the preparation of the material can be excluded to a certain extent if the synthesis of the materials is similar, like in the case of our materials. This allows a better focus on effects related to the dynamics of the support material like alloy formation and SMSI. When comparing CG and CA, it is noticeable that the Al component in CA exhibits a strong structural promoting effect, being able to keep the Cu-particles stabilized and mostly prevent sintering even after harsh treatment like a reduction at 480 °C. The Ga component in CG on the other hand is also able to prevent sintering to a certain degree. However, at elevated temperatures surface Cu becomes mobile and the structural promoting effect of the Ga components is lost, most likely due to its dynamic restructuring, which we did not observe with the Al components in CA. This dynamic behavior is somewhat similar to the Zn promotor widely described in literature. Generally, ZnO can be present in different forms (graphitic-like layers on Cu, (defective) wurtzite, surface $Zn^{\delta+}$ alloyed with Cu) depending mainly on the degree of reduction [59, 70–72]. Similarly, Ga oxide undergoes multiple transformations during reductive activation and under reaction conditions. In CG, the transformation toward the stable β-Ga_2O_3 phase at higher temperatures is predominant, similar to the thermal behavior known from $Ga(OH)_3$ gels. Similar thermal transformations occur in the Cu/ZnO catalyst during the calcination stage of the as-prepared catalyst. In both catalyst systems, there are indications that the formation of bulk alloys is not beneficial and not the major path of promotion. Different to the $GaPd_2$- and NiGa-systems, Ga does not easily form bulk alloys with Cu [26, 27]. However, bulk-alloying can be understood as the driving force for surface effects happening already at lower more relevant temperature. For Cu/ZnO, this is the well-known and widely discussed SMSI effect mentioned in the introduction. Indeed, for CG we observe that partial reduction occurs to some minor extent already upon reduction and similar as discussed for Cu/ZnO [10], it might be related to formation of a surface alloy. As for Cu/ZnO the stability of the surface alloy will depend on the reducing potential of the feed, i.e. the CO/CO_2 ratio. Dynamic and reversible de-alloying has been observed in particular in CO_2-and H_2O-rich feeds [21, 25]. The instability of a Cu_xGa_y surface alloy requires further systematic research and might be one reason, why we have not observed a very strong and clear promoting effect of our CG catalyst in CO_2 hydrogenation compared to unpromoted CA. Another possible explanation is that in our CG catalyst, we have employed relatively large amounts of Ga_2O_3, while recent literature for copper-based catalysts have reported only few percent of Ga_2O_3 to be efficient as promoter, which should not be overdosed [11–16]. While such loadings are not uncommon for promoters, this is in contrast to Cu/ZnO catalysts. In these systems, the oxide components fulfill both roles of a support and as a source for the reduced promoter species with less danger of spectator species. In fact, Cu/ZnO catalysts seem to rather provide as much promoter

as needed to form high-performance catalysts in a self-assembled manner in reducing atmosphere limited by the surface capacity of alloying. Such beneficial scenario might not be operational for Cu/Ga_2O_3, at least our attempt to simulate the Cu/ZnO catalyst at the industrially relevant 70:30 ratio in the Cu/Ga_2O_3 system did not easily form a highly active catalyst.

4 | Conclusion

In this work, a highly dispersed Cu/Ga_2O_3 catalyst containing large amounts of Ga (with a fixed molar Cu:M ratio of 70:30, similar to the well-known CuZn system) as well as a comparable reference sample containing Al_2O_3 instead was synthesized through the direct reduction of an LDH precursor. The simplicity of these systems and their similarity with the CuZn system, which also contains high amounts of promoter, allowed us to study the promoting effect of Ga as well as its dynamics.

The combination of operando XRPD, XANES, and EXAFS, as well as with DFT calculations, was a powerful approach to uncover the structural changes that occur in the CuGa system during activation and under reaction conditions. Using this approach, we disentangled the reduction of Ga^{3+} and phase changes, including changes in the coordination environment from octahedral to tetrahedral.

The results show that Ga responds dynamically to changing conditions, forming mostly octahedrally coordinated Ga_2O_3 during TPR, which is converted to a mixture of octahedrally and tetrahedrally coordinated Ga_2O_3 when the feed gas is applied. Furthermore, increasing the temperature to 480 °C led to a reduction of parts of Ga^{3+} to Ga^0 in the form of alloying with copper, which is accompanied by an increase in domain size. At 530 °C, further structural changes were observed. This allowed comparing the system to the CuZn system as a prototype for strong SMSI and dynamics in methanol synthesis. Unlike the CuZn-system, an excess of Ga and particularly the formation of bulk reduced Cu_xGa_y was not found to be beneficial. In the future, studying the dynamics of Ga at low dopant levels with preferential probing of the surface of the Cu particles and Cu-Ga entities would be helpful to further understand the mechanism behind Ga promotion. Furthermore, the dynamics could be deepened in the future by surface-sensitive XPS/LEIS and in situ TEM studies.

Acknowledgments

The authors gratefully acknowledge the funding from the SPP2080 (358713534) by the DFG (BE4767/3-2, GR3987/14-2, STU703/3-2) as well as financial support by KIT and the State of Schleswig-Holstein. The high-resolution scanning electron microscope with EDX detector was funded by the DFG (529613430, INST 257/717-1 FUGG). We acknowledge the MAX IV Laboratory for beamtime on the Balder beamline under proposal 20230387. Research conducted at MAX IV, a Swedish national user facility, is supported by Vetenskapsrådet (Swedish Research Council, VR) under contract 2018-07152, Vinnova (Swedish Governmental Agency for Innovation Systems) under contract 2018-04969, and Formas under contract 2019-02496. Claude Coppex, Jelena Jelic, and Felix Studt acknowledge the support of the state of Baden-Württemberg through bwHPC and the German Research Foundation (DFG) through grant number INST 40/575-1 FUGG (JUSTUS 2 cluster, RVs bw17D011). Support by the Helmholtz Association is also gratefully acknowledged. We thank Dr. Abhijeet Gaur for his advice regarding EXAFS modelling and fitting. We acknowledge TEM Center Kiel and especially Ulrich Schürmann for the TEM measurements. We thank Linda Klag (KIT-ITCP) for the discussion on the results. Finally, we acknowledge DAPHNE4NFDI (DFG project under project number 460248799) as well as further NFDI-consortia (NFDI4Cat, FAIRMAT, and NFDI4Chem) for fruitful discussion and valuable input for implementing FAIR data principles in this work.

Open access funding enabled and organized by Projekt DEAL.

Conflicts of Interest

The authors declare no conflicts of interest.

Data Availability Statement

The data that support the findings of this study are available in the Supporting Information of this article.

References

1. J. Burre, D. Bongartz, L. Brée, K. Roh, and A. Mitsos, "Power-to-X: Between Electricity Storage, E-Production, and Demand Side Management," *Chemie Ingenieur Technik* 92 (2020): 74–84, https://doi.org/10.1002/cite.201900102.

2. B. Rego de Vasconcelos and J.-M. Lavoie, "Recent Advances in Power-to-X Technology for the Production of Fuels and Chemicals," *Frontiers in chemistry* (2019): 7, https://doi.org/10.3389/fchem.2019.00392.

3. T. J. Deka, A. I. Osman, D. C. Baruah, and D. W. Rooney, "Methanol Fuel Production, Utilization, and Techno-Economy: A Review," *Environmental Chemistry Letters* 20 (2022): 3525–3554, https://doi.org/10.1007/s10311-022-01485-y.

4. S. G. Jadhav, P. D. Vaidya, B. M. Bhanage, and J. B. Joshi, "Catalytic Carbon Dioxide Hydrogenation to Methanol: A Review of Recent Studies," *Chemical Engineering Research and Design* 92 (2014): 2557–2567, https://doi.org/10.1016/j.cherd.2014.03.005.

5. M. Heenemann, M.-M. Millet, and F. Girgsdies, "The Mechanism of Interfacial CO_2 Activation on Al Doped Cu/ZnO," *ACS Catalysis* 10 (2020): 5672–5680, https://doi.org/10.1021/acscatal.0c00574.

6. E. Frei, A. Gaur, and H. Lichtenberg, "Activating a Cu/ZnO : Al Catalyst—Much More Than Reduction: Decomposition, Self-Doping and Polymorphism," *ChemCatChem* 11 (2019): 1587–1592, https://doi.org/10.1002/cctc.201900069.

7. B. Mockenhaupt, J. Gieser, and S. Najafishirtari, "On the Secondary Promotion Effect of Al and Ga on Cu/ZnO Methanol Synthesis Catalysts," *Journal of Catalysis* 439 (2024): 115785, https://doi.org/10.1016/j.jcat.2024.115785.

8. M. Kurtz, N. Bauer, and C. Büscher, "New Synthetic Routes to More Active Cu/ZnO Catalysts Used for Methanol Synthesis," *Catalysis Letters* 92 (2004): 49–52, https://doi.org/10.1023/B:CATL.0000011085.88267.a6.

9. R. van den Berg, G. Prieto, and G. Korpershoek, "Structure Sensitivity of Cu and CuZn Catalysts Relevant to Industrial Methanol Synthesis," *Nature Communications* 7 (2016): 13057, https://doi.org/10.1038/ncomms13057.

10. S. Kuld, M. Thorhauge, and H. Falsig, "Quantifying the Promotion of Cu Catalysts by ZnO for Methanol Synthesis," *Science* 352 (2016): 969–974, https://doi.org/10.1126/science.aaf0718.

11. E. L. Fornero, P. B. Sanguineti, D. L. Chiavassa, A. L. Bonivardi, and M. A. Baltanás, "Performance of Ternary $Cu–Ga_2O_3–ZrO_2$ Catalysts in the Synthesis of Methanol Using CO_2-Rich Gas Mixtures," *Catalysis Today* 213 (2013): 163–170.

12. C. Paris, A. Karelovic, and R. Manrique, "CO_2 Hydrogenation to Methanol With Ga- and Zn-Doped Mesoporous Cu/SiO_2 Catalysts Prepared by the Aerosol-Assisted Sol-Gel Process," *ChemSusChem* 13 (2020): 6409–6417, https://doi.org/10.1002/cssc.202001951.

13. A. M. Hengne, D. J. Yuan, N. S. Date, et al., "Preparation and Activity of Copper–Gallium Nanocomposite Catalysts for Carbon Dioxide Hydrogenation to Methanol," *Industrial & Engineering Chemistry Research* 58 (2019): 21331–21340.

14. M. M.-J. Li, Z. Zeng, F. Liao, X. Hong, and S. C. E. Tsang, "Enhanced CO_2 Hydrogenation to Methanol Over CuZn Nanoalloy in Ga Modified Cu/ZnO Catalysts," *Journal of Catalysis* 343 (2016): 157–167.

15. E. Lam, G. Noh, K. W. Chan, et al., "Enhanced CH_3OH Selectivity in CO_2 Hydrogenation Using Cu-based Catalysts Generated via SOMC From Ga III Single-sites," *Chemical Science* 11 (2020): 7593–7598.

16. D. Gómez, T. Vergara, M. Ortega, et al., "Interdependence between the Extent of Ga Promotion, the Nature of Active Sites, and the Reaction Mechanism Over Cu Catalysts for CO_2 Hydrogenation to Methanol," *ACS Catalysis* 14 (2024): 15265–15278.

17. D. Kordus, J. Timoshenko, and N. J. Divins, "Cu–Ga Interactions and Support Effects in CO_2 Hydrogenation to Methanol Catalyzed by Size-Controlled CuGa Nanoparticles Deposited on SiO_2 and ZnO," *ACS Catalysis* 15 (2025): 17241–17254, https://doi.org/10.1021/acscatal.5c03414.

18. M. Behrens, F. Studt, I. Kasatkin, et al., "The Active Site of Methanol Synthesis over $Cu/ZnO/Al_2O_3$ Industrial Catalysts," *Science* 336 (2012): 893–897.

19. H. Ham, S. W. Baek, C.-H. Shin, and J. W. Bae, "Roles of Structural Promoters for Direct CO_2 Hydrogenation to Dimethyl Ether Over Ordered Mesoporous Bifunctional $Cu/M–Al_2O_3$ (M = Ga or Zn)," *ACS Catalysis* 9 (2019): 679–690, https://doi.org/10.1021/acscatal.8b04060.

20. J. L. Alfke, M. Tejeda-Serrano, and S. Phadke, "Boundary Conditions for Promotion Versus Poisoning in Copper–Gallium-Based CO_2-to-Methanol Hydrogenation Catalysts," *ACS Catalysis* 14 (2024): 9166–9175, https://doi.org/10.1021/acscatal.4c01985.

21. M. Zabilskiy, V. L. Sushkevich, D. Palagin, M. A. Newton, F. Krumeich, and J. A. van Bokhoven, "The Unique Interplay Between Copper and Zinc During Catalytic Carbon Dioxide Hydrogenation to Methanol," *Nature Communications* 11 (2020): 2409, https://doi.org/10.1038/s41467-020-16342-1.

22. D. Laudenschleger, H. Ruland, and M. Muhler, "Identifying the Nature of the Active Sites in Methanol Synthesis Over $Cu/ZnO/Al_2O_3$ Catalysts," *Nature Communications* 11 (2020): 3898, https://doi.org/10.1038/s41467-020-17631-5.

23. N. J. Divins, D. Kordus, and J. Timoshenko, "Operando High-Pressure Investigation of Size-controlled CuZn Catalysts for the Methanol Synthesis Reaction," *Nature Communications* 12 (2021): 1435, https://doi.org/10.1038/s41467-021-21604-7.

24. R. Dalebout, L. Barberis, and G. Totarella, "Insight Into the Nature of the ZnOx Promoter During Methanol Synthesis," *ACS Catalysis* 12 (2022): 6628–6639, https://doi.org/10.1021/acscatal.1c05101.

25. J.-D. Grunwaldt, A. M. Molenbroek, N.-Y. Topsøe, H. Topsøe, and B. S. Clausen, "In Situ Investigations of Structural Changes in Cu/ZnO Catalysts," *Journal of Catalysis* 194 (2000): 452–460.

26. I. Sharafutdinov, C. F. Elkjær, and H. W. Pereira de Carvalho, "Intermetallic Compounds of Ni and Ga as Catalysts for the Synthesis of Methanol," *Journal of Catalysis* 320 (2014): 77–88, https://doi.org/10.1016/j.jcat.2014.09.025.

27. E. M. Fiordaliso, I. Sharafutdinov, H. W. P. Carvalho, et al., "Evolution of Intermetallic $GaPd_2/SiO_2$ Catalyst and Optimization for Methanol Synthesis at Ambient Pressure," *Science and Technology of Advanced Materials* 20 (2019): 521–531.

28. S. W. Lee, M. L. Luna, and N. Berdunov, "Unraveling Surface Structures of Gallium Promoted Transition Metal Catalysts in CO_2 Hydrogenation," *Nature Communications* 14 (2023): 4649, https://doi.org/10.1038/s41467-023-40361-3.

29. K. Nishi, K. Shimizu, and M. Takamatsu, "Deconvolution Analysis of Ga K-Edge XANES for Quantification of Gallium Coordinations in Oxide Environments," *The Journal of Physical Chemistry B* 102 (1998): 10190–10195, https://doi.org/10.1021/jp982704p.

30. N. M. Phadke, J. Van der Mynsbrugge, E. Mansoor, A. B. Getsoian, M. Head-Gordon, and A. T. Bell, "Characterization of Isolated Ga^{3+} Cations in Ga/H-MFI Prepared by Vapor-Phase Exchange of H-MFI Zeolite With $GaCl_3$," *ACS Catalysis* 8 (2018): 6106–6126, https://doi.org/10.1021/acscatal.8b01254.

31. Y. Chen, O. Sakata, and H. Morita, "Electronic States of Gallium Oxide Epitaxial Thin Films and Related Atomic Arrangement," *Applied Surface Science* 578 (2022): 151943, https://doi.org/10.1016/j.apsusc.2021.151943.

32. L. Li, J. A. Chalmers, S. R. Bare, S. L. Scott, and F. D. Vila, "Rigorous Oxidation State Assignments for Supported Ga-Containing Catalysts Using Theory-Informed X-ray Absorption Spectroscopy Signatures From Well-Defined Ga(I) and Ga(III) Compounds," *ACS Catalysis* 13 (2023): 6549–6561, https://doi.org/10.1021/acscatal.3c01021.

33. E. Kleymenov, J. Sa, and J. Abu-Dahrieh, "Structure of the Methanol Synthesis Catalyst Determined by In Situ HERFD XAS and EXAFS," *Catalysis Science & Technology* 2 (2012): 373–378, https://doi.org/10.1039/C1CY00277E.

34. A. I. Frenkel, J. A. Rodriguez, and J. G. Chen, "Synchrotron Techniques for In Situ Catalytic Studies: Capabilities, Challenges, and Opportunities," *ACS Catalysis* 2 (2012): 2269–2280.

35. A. Gaur, M. Schumann, and K. V. Raun, "Operando XAS/XRD and Raman Spectroscopic Study of Structural Changes of the Iron Molybdate Catalyst during Selective Oxidation of Methanol," *ChemCatChem* 11 (2019): 4871–4883, https://doi.org/10.1002/cctc.201901025.

36. A. Tsoukalou, P. M. Abdala, D. Stoian, et al., "Structural Evolution and Dynamics of an In_2O_3 Catalyst for CO_2 Hydrogenation to Methanol: An Operando XAS-XRD and In Situ TEM Study," *Journal of the American Chemical Society* 141 (2019): 13497–13505.

37. J.-D. Grunwaldt and B. S. Clausen, "Combining XRD and EXAFS With On-Line Catalytic Studies for In Situ Characterization of Catalysts," *Topics in Catalysis* 18 (2002): 37–43, https://doi.org/10.1023/A:1013838428305.

38. M. Behrens and R. Schlögl, "How to Prepare a Good Cu/ZnO Catalyst or the Role of Solid State Chemistry for the Synthesis of Nanostructured Catalysts," *Zeitschrift für Anorganische und Allgemeine Chemie* 639 (2013): 2683–2695, https://doi.org/10.1002/zaac.201300356.

39. S. Kühl, M. Friedrich, M. Armbrüster, and M. Behrens, "Cu, Zn, Al Layered Double Hydroxides as Precursors for Copper Catalysts in Methanol Steam Reforming—pH-controlled Synthesis by Microemulsion Technique," *Journal of Materials Chemistry* 22 (2012): 9632–9638.

40. J.-L. Gieser, *Hydrogenation of Carbon Dioxide in the Gas- and Liquid-Phase Over Cu-Based Catalysts* (University Duisburg-Essen, 2024).

41. N. S. Jamwal and A. Kiani, "Gallium Oxide Nanostructures: A Review of Synthesis, Properties and Applications," *Nanomaterials* 12 (2022): 2061.

42. K. Klementiev, K. Norén, S. Carlson, K. G. V. Sigfridsson Clauss, and I. Persson, "The BALDER Beamline at the MAX IV Laboratory," *Journal of Physics: Conference Series* 712 (2016): 012023.

43. A. A. Coelho, "TOPAS and TOPAS-Academic: An Optimization Program Integrating Computer Algebra and Crystallographic Objects Written in C++," *Journal of Applied Crystallography* 51 (2018): 210–218, https://doi.org/10.1107/S1600576718000183.

44. B. Ravel and M. Newville, "ATHENA, ARTEMIS , HEPHAESTUS: Data Analysis for X-ray Absorption Spectroscopy Using IFEFFIT," *Journal of Synchrotron Radiation* 12 (2005): 537–541, https://doi.org/10.1107/S0909049505012719.

45. G. Kresse and J. Furthmüller, "Efficient Iterative Schemes for Ab Initio Total-Energy Calculations Using a Plane-Wave Basis Set," *Physical Review B* 54 (1996): 11169–11186, https://doi.org/10.1103/PhysRevB.54.11169.

46. G. Kresse and J. Furthmüller, "Efficiency of Ab-Initio Total Energy Calculations for Metals and Semiconductors Using a Plane-Wave Basis

Set," *Computational Materials Science* 6 (1996): 15–50, https://doi.org/10.1016/0927-0256(96)00008-0.

47. A. Hjorth Larsen, J. Jørgen Mortensen, J. Blomqvist, et al., "The Atomic Simulation Environment—A Python Library for Working With Atoms," *Journal of Physics: Condensed Matter* 29 (2017): 273002.

48. G. Kresse and D. Joubert, "From Ultrasoft Pseudopotentials to the Projector Augmented-Wave Method," *Physical Review B* 59 (1999): 1758–1775, https://doi.org/10.1103/PhysRevB.59.1758.

49. P. E. Blöchl, "Projector Augmented-Wave Method," *Physical Review B* 50 (1994): 17953–17979.

50. J. Wellendorff, K. T. Lundgaard, and A. Møgelhøj, "Density Functionals for Surface Science: Exchange-Correlation Model Development With Bayesian Error Estimation," *Physical Review B* 85 (2012): 235149, https://doi.org/10.1103/PhysRevB.85.235149.

51. A. Jain, S. P. Ong, and G. Hautier, "Commentary: The Materials Project: A Materials Genome Approach to Accelerating Materials Innovation," *APL Materials* 1 (2013): 011002, https://doi.org/10.1063/1.4812323.

52. H. J. Monkhorst and J. D. Pack, "Special Points for Brillouin-Zone Integrations," *Physical Review B* 13 (1976): 5188–5192, https://doi.org/10.1103/PhysRevB.13.5188.

53. S. V. Krivovichev, V. N. Yakovenchuk, E. S. Zhitova, A. A. Zolotarev, Y. A. Pakhomovsky, and G. Y. Ivanyuk, "Crystal Chemistry of Natural Layered Double Hydroxides. 2. Quintinite-1 M: First Evidence of a Monoclinic Polytype in M^{2+}-M^{3+} Layered Double Hydroxides," *Mineralogical Magazine* 74 (2010): 833–840, https://doi.org/10.1180/minmag.2010.074.5.833.

54. G. C. Bond, S. N. Namijo, and J. S. Wakeman, "Thermal Analysis of Catalyst Precursors," *Journal of Molecular Catalysis* 64 (1991): 305–319, https://doi.org/10.1016/0304-5102(91)85140-W.

55. S. Kühl, A. Tarasov, S. Zander, I. Kasatkin, and M. Behrens, "Cu-Based Catalyst Resulting From a Cu,Zn,Al Hydrotalcite-Like Compound: A Microstructural, Thermoanalytical, and In Situ XAS Study," *Chemistry – A European Journal* 20 (2014): 3782–3792.

56. P. Kappen, J.-D. Grunwaldt, B. S. Hammershøi, L. Tröger, and B. S. Clausen, "The State of Cu Promoter Atoms in High-Temperature Shift Catalysts—An In Situ Fluorescence XAFS Study," *Journal of Catalysis* 198 (2001): 56–65.

57. I.-K. Suh, H. Ohta, and Y. Waseda, "High-Temperature Thermal Expansion of Six Metallic Elements Measured by Dilatation Method and X-ray Diffraction," *Journal of Materials Science Letters* 23 (1988): 757–760.

58. S. Geller, "Crystal Structure of β-Ga_2O_3," *The Journal of Chemical Physics* 33 (1960): 676–684.

59. T. Lunkenbein, J. Schumann, M. Behrens, R. Schlögl, and M. G. Willinger, "Formation of a ZnO Overlayer in Industrial Cu/ZnO/Al_2O_3 Catalysts Induced by Strong Metal–Support Interactions," *Angewandte Chemie* 127 (2015): 4627–4631.

60. E. J. Mittemeijer and P. Scardi, *Diffraction Analysis of the Microstructure of Materials* (Springer Science & Business Media, 2013).

61. A. Sharma, M. Varshney, and H. Saraswat, "Nano-Structured Phases of Gallium Oxide (GaOOH, α-Ga_2O_3, β-Ga_2O_3, γ-Ga_2O_3, δ-Ga_2O_3, and ε-Ga_2O_3): Fabrication, Structural, and Electronic Structure Investigations, Structural, and Electronic Structure Investigations," *International Nano Letters* 10 (2020): 71–79, https://doi.org/10.1007/s40089-020-00295-w.

62. F. Behafarid and B. R. Cuenya, "Towards the Understanding of Sintering Phenomena at the Nanoscale: Geometric and Environmental Effects," *Topics in Catalysis* 56 (2013): 1542–1559, https://doi.org/10.1007/s11244-013-0149-4.

63. B. J. O'Neill, J. T. Miller, P. J. Dietrich, F. G. Sollberger, F. H. Ribeiro, and J. A. Dumesic, "Operando X-ray Absorption Spectroscopy Studies of Sintering for Supported Copper Catalysts During Liquid-Phase Reaction," *ChemCatChem* 6 (2014): 2493–2496.

64. J. Jaumot, A. de Juan, and R. Tauler, "MCR-ALS GUI 2.0: New Features and Applications," *Chemometrics and Intelligent Laboratory Systems* 140 (2015): 1–12, https://doi.org/10.1016/j.chemolab.2014.10.003.

65. M. Behrens, S. Zander, and P. Kurr, "Performance Improvement of Nanocatalysts by Promoter-Induced Defects in the Support Material: Methanol Synthesis Over Cu/ZnO:Al," *Journal of the American Chemical Society* 135 (2013): 6061–6068, https://doi.org/10.1021/ja310456f.

66. C. Otero Areán, A. L. Bellan, M. P. Mentruit, M. R. Delgado, and G. T. Palomino, "Preparation and Characterization of Mesoporous γ-Ga_2O_3," *Microporous and Mesoporous Materials* 40 (2000): 35–42, https://doi.org/10.1016/S1387-1811(00)00240-7.

67. L. Li, W. Wei, and M. Behrens, "Synthesis and Characterization of α-, β-, and γ-Ga_2O_3 Prepared From Aqueous Solutions by Controlled Precipitation," *Solid State Sciences* 14 (2012): 971–981, https://doi.org/10.1016/j.solidstatesciences.2012.04.037.

68. E. van Steen, M. Claeys, M. E. Dry, J. van de Loosdrecht, E. L. Viljoen, and J. L. Visagie, "Stability of Nanocrystals: Thermodynamic Analysis of Oxidation and Re-reduction of Cobalt in Water/Hydrogen Mixtures," *The Journal of Physical Chemistry B* 109 (2005): 3575–3577.

69. M. L. Schulte, V. Truttmann, D. E. Doronkin, et al., "Monitoring the Fate of Zn in the Cu/ZnO/ZrO_2 Catalyst during CO_2-to-Methanol Synthesis at High Conversions by Operando Spectroscopy," *Angewandte Chemie* 137 (2025): e202423281.

70. A. Urakawa, "Mind the Gaps in CO_2-to-Methanol," *Nature Catalysis* 4 (2021): 447–448.

71. C. Holse, C. F. Elkjær, and A. Nierhoff, "Dynamic Behavior of CuZn Nanoparticles Under Oxidizing and Reducing Conditions," *The Journal of Physical Chemistry C* 119 (2015): 2804–2812, https://doi.org/10.1021/jp510015v.

72. G. Pacchioni, "From CO_2 to Methanol on Cu/ZnO/Al_2O_3 Industrial Catalyst. What Do We Know About the Active Phase and the Reaction Mechanism?," *ACS Catalysis* 14 (2024): 2730–2745, https://doi.org/10.1021/acscatal.3c05669.

73. G. Landrot and E. Fonda, "Fastosh: A Software for the Treatment of XAFS Datasets of Environmental Relevance or Acquired in Operando Conditions," *Journal of Synchrotron Radiation* 32 (2025): 1085–1094, https://doi.org/10.1107/S1600577525003923.

74. G. Tunell, E. Posnjak, and C. J. Ksanda, "Geometrical and Optical Properties, and Crystal Structure of Tenorite," *Zeitschrift für Kristallographie—Crystalline Materials* 90 (1935): 120–142, https://doi.org/10.1524/zkri.1935.90.1.120.

75. J. M. Rubio González and C. Otero Areán, "X-Ray Diffraction Determination of the Cation Distribution and Oxygen Positional Parameter in Polycrystalline Spinels," *Journal of the Chemical Society, Dalton Transactions* 1985 (1985): 2155–2159, https://doi.org/10.1039/DT9850002155.

76. F. Weibke, "Das Zustandsdiagramm Des Systems Kupfer–Gallium" *Zeitschrift für anorganische und allgemeine Chemie* 220, (1934): 293–311.

77. A. Kirfel and K. Eichhorn, "Accurate Structure Analysis With Synchrotron Radiation. The Electron Density in Al_2O_3 and Cu_2O," *Acta Crystallographica Section A Foundations of Crystallography* 46 (1990): 271–284, https://doi.org/10.1107/S0108767389012596.

78. R. Tauler, "Multivariate Curve Resolution Applied to Second Order Data," *Chemometrics and Intelligent Laboratory Systems* 30 (1995): 133–146, https://doi.org/10.1016/0169-7439(95)00047-X.

79. R. Tauler, A. Smilde, and B. Kowalski, "Selectivity, Local Rank, Three-Way Data Analysis and Ambiguity in Multivariate Curve Resolution," *Journal of Chemometrics* 9 (1995): 31–58, https://doi.org/10.1002/cem.1180090105.

80. R. Wyckoff, "Crystal Structure," *Am Miner Cryst Structure Database* 2 (1963): 7–83.

81. J. Åhman, G. Svensson, and J. Albertsson, "A Reinvestigation of β-Gallium Oxide," *Acta Cryst C* 52 (1996): 1336–1338.

82. B. Yao, A. M. Wang, and B. Z. Ding, "Study on Structure of a New Binding Phase in Polycrystalline Diamond," *Journal of Materials Science Letters* 14 (1995): 931–933, https://doi.org/10.1007/BF02427468.

Supporting Information

Additional supporting information can be found online in the Supporting Information section.

In the Supporting Information, we provide additional information to the main manuscript. This includes some more experimental details, ex situ characterization, synchrotron measurements, and XAS spectra fitting and analysis. Furthermore, the Supporting Information includes additional results from DFT calculations and details on Cu_xGa_y structures obtained by DFT. The authors have cited additional references within the Supporting Information [42–44, 57, 58, 64, 73–82].

Supporting File: cctc70510-sup-0001-SuppMat.pdf.